Dalton Transactions

ROYAL SOCIETY OF CHEMISTRY

PAPER

View Article Online
View Journal | View Issue

Cite this: *Dalton Trans.*, 2024, **53**, 17281

Modulating quantum tunnelling of magnetization in Dy isotopologue dimers†

Ting-Ting Ruan,[a] Eufemio Moreno-Pineda, *[b,c,d] Sagar Paul, [d] Michael Schulze,[d] Sören Schlittenhardt, [a] Asato Mizuno, [e] Wolfgang Wernsdorfer *[d] and Mario Ruben *[a,f,g]

Received 18th June 2024,
Accepted 26th September 2024

DOI: 10.1039/d4dt01769b

rsc.li/dalton

Qudits are anticipated to streamline quantum computation by minimizing iterations, lowering error rates, and facilitating error correction. It has been shown that Dy(III)-based molecular systems can act as qudits with expanded Hilbert spaces. Achieving a robust intramolecular interaction, whether exchange or dipolar, is crucial for spanning the Hilbert space of qudits; hence, short Dy(III)···Dy(III) distances are required. Looking for multilevel systems that can be employed as qudits, we have synthesized and characterized two dysprosium-based isotopologues: $[^{163}Dy_2(BTFA)_4(PHZP)_2]^0$ (**1**$^{(I=5/2)}$) and $[^{164}Dy_2(BTFA)_4(PHZP)_2]^0$ (**2**$^{(I=0)}$), where BTFA = 3-benzoyl-1,1,1-trifluoroacetone and PHZP = *N*′-[(*E*)-(pyrazin-2-yl)methylidene]pyrazine-2-carbohydrazonate. Both complexes showed slow magnetic relaxation at zero applied magnetic field. μSQUID investigations, at milli-Kelvin temperatures, and direct and alternating current magnetic measurements reveal distinctions in the magnetic behavior between the two complexes and an operative interaction between the Dy(III) centers. We find that the presence or absence of the nuclear spin plays a minor role in the magnetic properties above 2 K. On the contrary, at milli-Kelvin temperatures, μSQUID studies show enhanced relaxation in **1**$^{(I=5/2)}$, attributed to several quantum tunnelling pathways enabled by hyperfine and quadrupole interactions. The interplay between the antiferromagnetic coupling and enhanced relaxation indicates that the exchange coupling influences the relaxation mechanisms at different temperature ranges.

Introduction

The study of Single-Molecule Magnets (SMMs) has witnessed significant advancements in recent decades, driven by the quantum nature of their magnetic properties and their potential applications in quantum computing[1–4] and spintronics.[5–7] Lanthanides, such as Dy(III), Tb(III), Ho(III), and Er(III), have particularly gained prominence due to their substantial magnetic anisotropy and large magnetic moment.[8–12] Additionally, lanthanide-based SMMs (Ln-SMMs) have been suggested as frameworks for Quantum Information Processing (QIP) schemes,[13–17] functioning as quantum bits (qubits) or qu*d*its. This proposition was validated by implementing a quantum algorithm,[18] in a single molecular unit from the prototypical $[TbPc_2]^0$ SMM, incorporated within a hybrid spintronic structure.[13,15,19]

The magnetization dynamics of Ln-SMMs result in magnetic bistability, which is essential for their potential applications. The factors influencing the magnetization dynamics of SMMs are complex, with the magnetic anisotropy of the spin carriers and their interactions being the most important parameters. Typically, the intrinsic nature of the f-electrons, shielded by the outer shell electrons, is responsible for the weak magnetic interactions between the lanthanide centers. However, interactions and anisotropy have been shown to

[a]*Institute of Nanotechnology (INT), Karlsruhe Institute of Technology (KIT), Hermann-von-Helmholtz-Platz 1, D-76344 Eggenstein-Leopoldshafen, Germany. E-mail: mario.ruben@kit.edu*
[b]*Universidad de Panamá, Facultad de Ciencias Naturales, Exactas y Tecnología, Depto. de Química-Física, Panamá, 0824, Panamá. E-mail: eufemio.moreno@up.ac.pa*
[c]*Universidad de Panamá, Facultad de Ciencias Naturales, Exactas y Tecnología, Grupo de Investigación de Materiales, Panamá, 0824, Panamá*
[d]*Physikalisches Institut, Karlsruhe Institute of Technology (KIT), Engesserstraße 15, D-76131 Karlsruhe, Germany. E-mail: wolfgang.wernsdorfer@kit.edu*
[e]*Division of Chemistry, Department of Materials Engineering Science, Graduate School of Engineering Science, Osaka University, 1-3 Machikaneyama, Toyonaka, Osaka 560-8531, Japan*
[f]*Institute of Quantum Materials and Technologies (IQMT), Karlsruhe Institute of Technology (KIT), Hermann-von-Helmholtz-Platz 1, D-76344 Eggenstein-Leopoldshafen, Germany*
[g]*Centre Européen de Sciences Quantiques (CESQ), Institutde Science et d'Ingénierie Supramoléculaires (ISIS), 8 allée Gaspard Monge, BP 70028, 67083 Strasbourg Cedex, France*

†Electronic supplementary information (ESI) available. CCDC 2337590 and 2337589. For ESI and crystallographic data in CIF or other electronic format see DOI: https://doi.org/10.1039/d4dt01769b

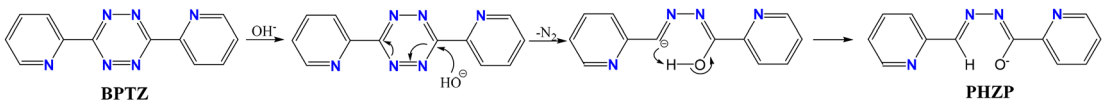

Scheme 1 The possible mechanism of hydrolysis process of the ligand from 3,6-dipyrazin-2-yl-1,2,4,5-tetrazine (BPTZ, left) to *N*′-[(*E*)-pyrazin-2-yl) methylidene]pyrazine-2-carbohydrazonate (PHZP, right).

influence the relaxation dynamics of multinuclear lanthanide SMMs.[20–26]

Upon reviewing the literature related to SMMs, we were prompted to focus more on systems wherein magnetic units are linked through bridging ligands to form high-dimensional frameworks.[27] In such molecules, the selection of organic moieties (ligands) is meticulous, aiming to adjust the physical properties of the resulting compounds.[28–30] Our research team has successfully synthesized two dinuclear dysprosium SMMs with isotopic enrichment, using a highly π-conjugated polyheteroaromatic molecule as a bridging ligand.[23] The findings presented in the study demonstrated that the strength of the intramolecular interaction (exchange or dipolar) is a crucial factor for spanning the Hilbert space of qu*d*its, foreseeing a preference for shorter Dy(III)···Dy(III) configurations.[23]

The group of ligands based on 1,2,4,5-tetrazine[31–34] is noteworthy in coordination chemistry due to their easy functionalization and redox activity, which can augment magnetic communication among metal ions.[35–38] In this context, the ligand 3,6-dipyrazin-2-yl-1,2,4,5-tetrazine (BPTZ) emerges as an appealing choice. By introducing isotopically enriched ^{163}Dy(III) and ^{164}Dy(III), we attempted the syntheses of BPTZ-based Dy(III) complexes. To our surprise, instead of obtaining two BPTZ-containing compounds, we discovered the creation of two distinct isotopologues: $[^{163}Dy_2(BTFA)_4(PHZP)_2]^0$ ($\mathbf{1}^{(I=5/2)}$) and $[^{164}Dy_2(BTFA)_4(PHZP)_2]^0$ ($\mathbf{2}^{(I=0)}$). The BPTZ ligand was found to have been transformed into a new ligand, *N*′-[(*E*)-pyrazin-2-yl) methylidene]pyrazine-2-carbohydrazonate (PHZP), as illustrated in Scheme 1. The two complexes showed SMM characteristics at zero applied magnetic field. We investigate the impact of the metal–metal distance on the intramolecular interaction as well as the effect of the nuclear spins on the dynamic properties of two dinuclear Dy(III)-SMMs through studies involving AC magnetic susceptibility and single crystal μSQUID data conducted at sub-Kelvin temperatures. We find similar relaxation behaviors down to 2 K temperature for both systems, which is a direct consequence of the short Dy(III)···Dy(III) distance-enhancing the intramolecular interaction (exchange or dipolar). However, low-temperature μSQUIDs investigations of the magnetization reversal reveal significant differences in the relaxation mechanism between the two isotopologues (I = 0, 5/2).

Results and discussion

Syntheses and structures

Complexes $\mathbf{1}^{(I=5/2)}$ and $\mathbf{2}^{(I=0)}$ were obtained by reacting one equivalent of ligand BPTZ with two equivalents of Ln(BTFA)$_3$(H$_2$O)$_2$ precursor, in which Ln = ^{163}Dy(III) (I = 5/2) for $\mathbf{1}^{(I=5/2)}$ and ^{164}Dy(III) (I = 0) for $\mathbf{2}^{(I=0)}$, respectively (see ESI† for details). Crystals of $\mathbf{1}^{(I=5/2)}$ and $\mathbf{2}^{(I=0)}$, suitable for single crystal X-ray studies, were grown from a mixture of ethanol and dichloromethane. X-ray single crystal studies reveal both complexes to be isomorphic, crystallizing in the triclinic $P\bar{1}$ space group with two symmetry-related molecules residing in the unit cell (Fig. 1c).

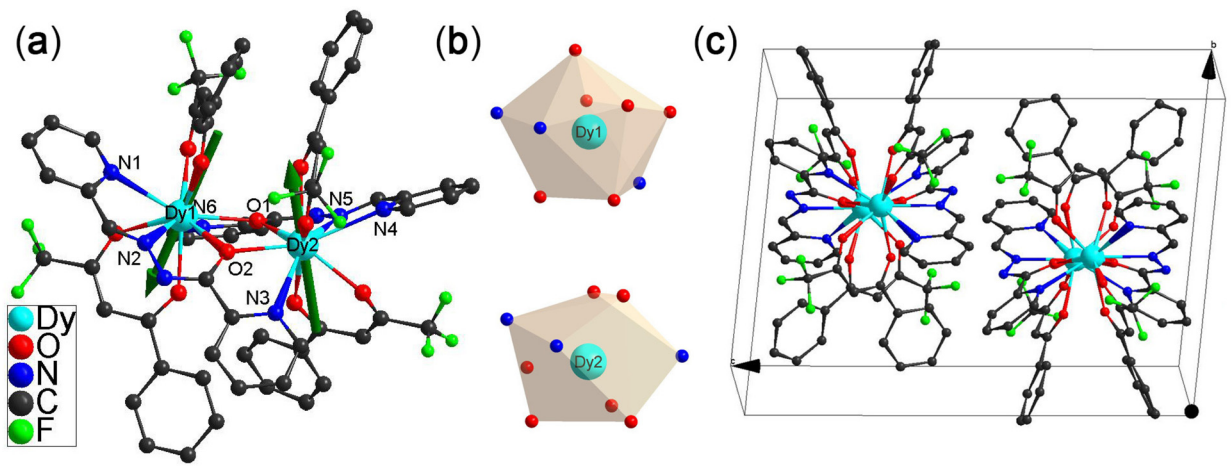

Fig. 1 (a) Crystal structure of $[Dy_2(BTFA)_4(PHZP)_2]$. The green arrows represent the anisotropy axis for each Dy(III) obtained from *ab initio* CASSCF calculations; (b) polyhedral representation of the Dy(III); (c) unit cell of $[Dy_2(BTFA)_4(PHZP)_2]$ showing the two molecules residing in the unit cell, related by an inversion center.

The ligand BPTZ is highly susceptible to nucleophilic attack by OH^-, causing the opening of the tetrazine ring and generating the asymmetrical *N*′-[(*E*)-pyrazin-2-yl)methylidene]pyrazine-2-carbohydrazonate (PHZP) ligand (Scheme 1).[39–41] Both Dy(III) ions are bridged by two PHZP ligands. Each Dy(III) coordinates in a tridentate chelating mode (N1, N2, and O2) with one of the ligands and a bidentate mode with the second ligand (O1 and N6). Two BTFA units complete the coordination sphere, forming a N_3O_6 nine-coordinated environment around each metal center (Fig. 1a). The Dy–O and Dy–N bond lengths are in the range of 2.325(3)–2.460(3) Å and 2.497(3)–2.721(3) Å for $\mathbf{1}^{(I=5/2)}$ and 2.325(2)–2.460(2) Å and 2.485(3)–2.712(3) Å for $\mathbf{2}^{(I=0)}$, respectively. The amide oxygen atoms (O1 and O2) within the PHZP ligands form bonds in the deprotonated imidic acid mode (O^-), acting as bridges between the two Dy (III) ions and resulting in the formation of a Dy_2O_2 quadrilateral geometry. The Dy1–O–Dy2 angles are 115.7° for $\mathbf{1}^{(I=5/2)}$ and $\mathbf{2}^{(I=0)}$. The intramolecular Dy···Dy distance for $\mathbf{1}^{(I=5/2)}$ and $\mathbf{2}^{(I=0)}$ is 4.065(5) Å and 4.064(3) Å, respectively. Analysis of the degree of distortion of the coordination environment of the lanthanides is performed using SHAPE,[42] resulting in different N_3O_6 environments for Dy1 and Dy2 for $\mathbf{1}^{(I=5/2)}$ and $\mathbf{2}^{(I=0)}$ (Table S2†). The nine-coordinated Dy1 ions in both $\mathbf{1}^{(I=5/2)}$ and $\mathbf{2}^{(I=0)}$ represent a spherical tricapped trigonal prism motif with the same D_{3h} symmetry, and the continuous shape measure (CShM) values are determined to be 1.885 and 1.858, respectively. Dy2 in $\mathbf{1}^{(I=5/2)}$ and $\mathbf{2}^{(I=0)}$ ions represent the uniform Muffin arrangement with the same C_s symmetry, and the continuous shape measure (CShM) values are determined to be 2.253 and 2.250, respectively (Fig. 1b).

The purity of the phases in the polycrystalline samples of $\mathbf{1}^{(I=5/2)}$ and $\mathbf{2}^{(I=0)}$ was assessed through powder X-ray diffraction (PXRD) analysis. The observed PXRD patterns for both $\mathbf{1}^{(I=5/2)}$ and $\mathbf{2}^{(I=0)}$ demonstrated good agreement with the simulated patterns (Fig. S2†), indicating that both samples consist of a single crystalline phase.

Magnetic properties

Static magnetic studies. The static magnetic susceptibility studies for both complexes were carried out on polycrystalline samples with a DC field of 1 kOe, in a temperature range from 2 K to 300 K (Fig. 2). At room temperature, the experimental $\chi_M T$ values are 28.1 cm^3 K mol^{-1} for $\mathbf{1}^{(I=5/2)}$ and 28.4 cm^3 K mol^{-1} for $\mathbf{2}^{(I=0)}$, respectively. These results agree with the anticipated values for two uncoupled Dy(III) ions (with J = 15/2 and g_J = 4/3). The $\chi_M T$ products gradually decreased until reaching around 20 K, after which a rapid decline occurred, ultimately reaching 15.2 cm^3 K mol^{-1} for $\mathbf{1}^{(I=5/2)}$ and 16.3 cm^3 K mol^{-1} for $\mathbf{2}^{(I=0)}$ at the lowest temperature of 2 K. This observation can be attributed to the depopulation of the excited Stark sublevels and antiferromagnetic exchange coupling between the two Dy(III) ions in the complexes (*vide infra*).

The magnetization-field curves ($M(H)$) for both complexes were also examined within the magnetic field range of 0 to 7 T and a temperature range of 2 to 5 K, revealing a swift rise at low magnetic fields, as depicted in the insets of Fig. 2. At high magnetic fields, the magnetization shows near horizontal behaviour, with recorded values of 10.1μ_B for $\mathbf{1}^{(I=5/2)}$ and 10.4μ_B for $\mathbf{2}^{(I=0)}$, at 7 T. These $M(H)$ values closely align with the anticipated values for two Dy(III) ions featuring a well-defined J = 15/2 ground doublet, approximately ~10μ_B.

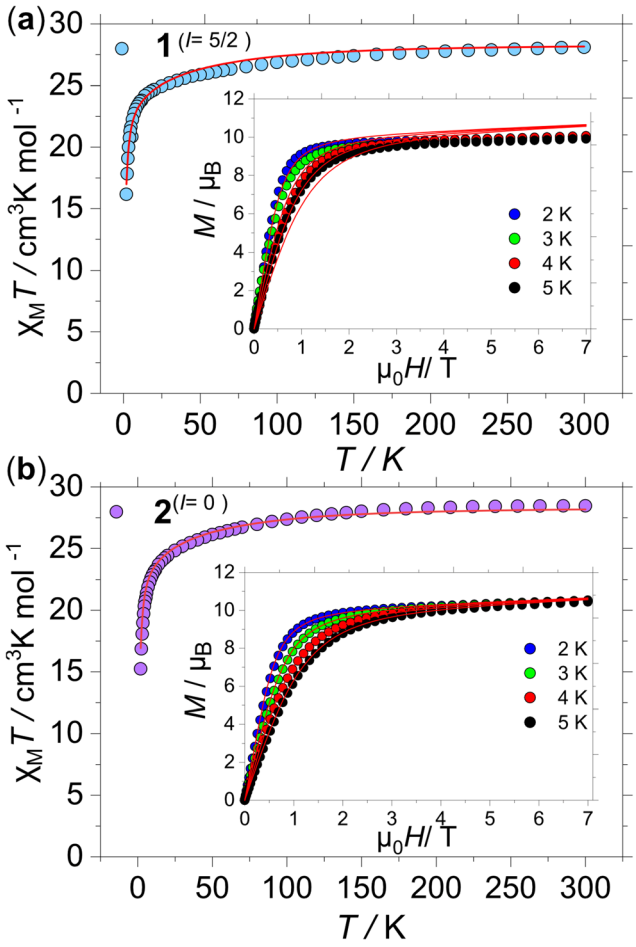

Fig. 2 The $\chi_M T$ *vs.* T plots for compounds (a) $\mathbf{1}^{(I=5/2)}$ and (b) $\mathbf{2}^{(I=0)}$. Inset: $M(H)$ data at different temperatures. Solid lines are the fits using the CF parameters obtained from CASSCF calculations as described in the main text.

Dynamic magnetic properties. To investigate the magnetization dynamics, alternating current (AC) magnetic susceptibilities studies were conducted. Both complexes display the distinctive SMM signature at zero applied magnetic field. Contrary to the observation in other isotopologue complexes,[23,43,44] the AC susceptibilities for $\mathbf{1}^{(I=5/2)}$ and $\mathbf{2}^{(I=0)}$ are quasi-superimposable as shown in Fig. S6.† For both complexes, we find that at the lowest temperature (2 K), a maximum is observed at 180 Hz in the out-of-phase component (χ''_M), which slowly shifts towards higher frequencies with increasing temperature up to 8 K. Employing a generalized Debye model, the symmetric semicircle Cole–Cole data are fitted between 2 and 6.8 K (Fig. S4 and S4†). This fitting process allows for the extraction of relaxation times (τ) and the distribution of relaxation times (α values): 0.05(3) < α < 0.18(4)

for $\mathbf{1}^{(I=5/2)}$, $0.04(3) < \alpha < 0.14(6)$ for $\mathbf{2}^{(I=0)}$, tending to be larger at lower temperatures (Fig. S3 and S4†). This observation suggests a relatively narrow distribution of relaxation times for $\mathbf{1}^{(I=5/2)}$ and $\mathbf{2}^{(I=0)}$. The temperature dependence of the relaxation times ($\tau(T)$) is practically equal for both complexes (see Fig. 3b, d, S6 and S7†) and can be effectively fitted using the following eqn (1):

$$\tau^{-1} = \tau_0^{-1} \exp(-U_{\text{eff}}/k_{\text{B}}T) + CT^n + \tau_{\text{QTM}}^{-1} \quad (1)$$

where the first term is the rate of Orbach process, the second one corresponds to the Raman process and the third term is the rate of Quantum Tunneling of the Magnetization (QTM). The best-fit yields values of U_{eff} = 37(1) K (26(1) cm^{-1}), τ_0 = 8(1) × 10^{-7} s, C = 28(6) s^{-1} K^{-n}, n = 2.4(2), τ_{QTM} = 1.01(1) × 10^{-4} s, R^2 = 2.2 × 10^{-4} for $\mathbf{1}^{(I=5/2)}$, and U_{eff} = 41(2) K (28(1) cm^{-1}), τ_0 = 7(1) × 10^{-7} s, C = 9(1) s^{-1} K^{-n}, n = 3.2(1) and τ_{QTM} = 9.2(1) × 10^{-4} s, R^2 = 1.4 × 10^{-4} for $\mathbf{2}^{(I=0)}$ (Fig. S7a and b†). As anticipated from a straightforward examination of their χ''_{M} profiles, the relaxation parameters are nearly identical. Note that the n parameter of the Raman process was found to be small.[45,46] Low Raman n parameters have been ascribed to low vibrational modes,[47] which can be better described by the sum of contributions arising from phonon modes, with the second term in (1) being replaced by:

$$\tau_{\text{Raman}}^{-1} = \sum_{i=1}^{2} C_i \frac{\exp\left(\frac{\hbar\omega_i}{k_{\text{B}}T}\right)}{\left(\exp\left(\frac{\hbar\omega_i}{k_{\text{B}}T}\right) - 1\right)^2} \quad (2)$$

In (2) the ω_i describe the active vibrational modes. The best fit requires the inclusion of a single vibrational mode, yielding U_{eff} = 29.9(7) K (20.8(5) cm^{-1}), τ_0 = 1.4(1) × 10^{-6} s, C_1 = 1497(783) s^{-1}, ω_1 = 3.8(9) cm^{-1}, τ_{QTM} = 9.8(2) × 10^{-4} s, R^2 = 1.9 × 10^{-4} for $\mathbf{1}^{(I=5/2)}$, and U_{eff} = 30.1(1) K (20.9(6) cm^{-1}), τ_0 = 1.5(2) × 10^{-5} s, C_1 = 65 542(1064) s^{-1}, ω_1 = 6.4(4) cm^{-1}, τ_{QTM} = 9.0(6) × 10^{-4} s, R^2 = 1.8 × 10^{-4} (Fig. 3b and d). The ω_i are found to be low, as expected for molecular systems.[45,48,49]

Sub-Kelvin μSQUID studies. Strikingly, although dynamic magnetic studies demonstrated the anticipated SMM characteristics under zero DC field of the isotopologues, a clear distinction between the two isotopologues was not perceptible as previously observed in comparable isotopologue studies.[23,43,44,49–56] To explore the variations in the relaxation dynamics and the nuclear spin effects, magnetic hysteresis curves were measured employing a μSQUID array down to sub-Kelvin

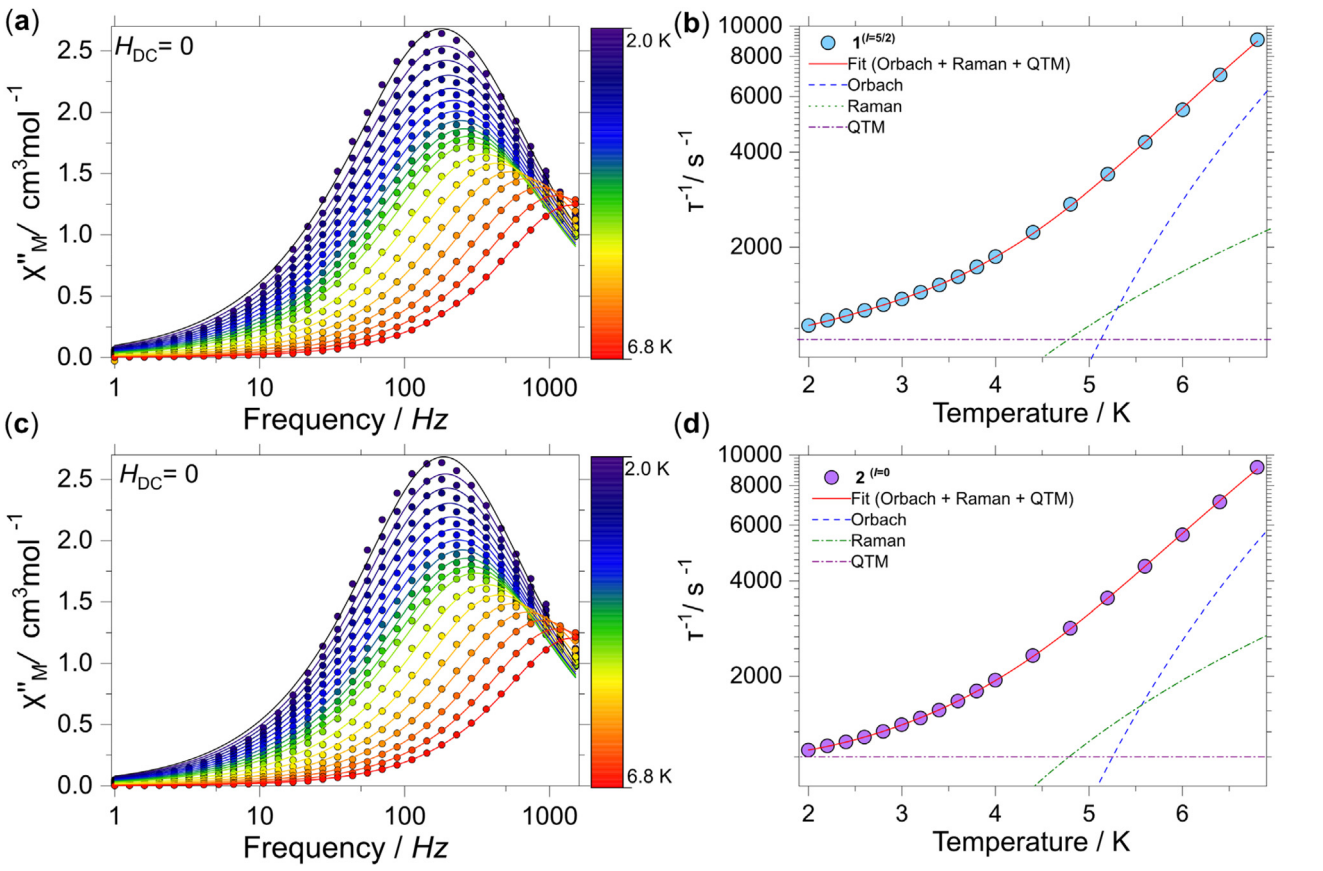

Fig. 3 Experimental frequency-dependent magnetic susceptibility data at zero applied DC (H_{DC}) field and variable temperatures ($\chi''_{\text{M}}(\nu)$) for (a) $\mathbf{1}^{(I=5/2)}$ and (b) $\mathbf{2}^{(I=0)}$; (c) temperature dependence of the magnetic relaxation time $\tau(T)$ under zero field for $\mathbf{1}^{(I=5/2)}$ (pale blue) and $\mathbf{2}^{(I=0)}$ (light orange). The solid red lines in panels are the best fit to eqn (1) with the second term being that given in eqn (2), consisting of the Orbach and Raman relaxation processes, while the dashed and dashed-dotted lines are the decomposition for each process.

temperatures. The studies were carried out on single crystals of $\mathbf{1}^{(I=5/2)}$ and $\mathbf{2}^{(I=0)}$, with the field applied along the principal anisotropic axis.[57] Hysteresis loops were obtained at different sweep rates and temperatures, ranging from 5 K to 30 mK and from 0.5 to 64 mT s^{-1} (Fig. 4). Well-defined two-step hysteresis loops were obtained for complexes $\mathbf{1}^{(I=5/2)}$ and $\mathbf{2}^{(I=0)}$, with the width of the loops increasing as the temperatures decreased and the sweep rates increased, confirming the SMM behavior.

The hysteresis loops are a common feature for two Ising-like spins that are antiferromagnetically coupled: around zero field, they exhibit an S-shaped curve with two tunnel steps at positive and negative fields.[44,58,59] The presence of S-shaped loops and the observation of the tunnel steps for $\mu_0 H_z < \pm 0.2$ T suggest the existence of two antiferromagnetically coupled Dy(III) ions within the system. The occurrence of these steps is attributed to the transition from parallel (ferromagnetic) to antiparallel (antiferromagnetic) alignment of the Dy(III) anisotropic moments. An additional step is observed at zero field, which corresponds to the pinning of some molecules to the ferromagnetic state.[44,60,61] Upon comparing the hysteresis curves for $\mathbf{1}^{(I=5/2)}$ and $\mathbf{2}^{(I=0)}$, it is apparent that the nuclear spin-bearing system results in narrower loops, signifying a more effective relaxation mechanism, as previously observed.[44]

Theoretical calculations. For a deeper understanding of the magnetic relaxation mechanisms in $\mathbf{1}^{(I=5/2)}$ and $\mathbf{2}^{(I=0)}$, we conducted Complete-Active-Space Self-Consistent Field (CASSCF) calculations on the binuclear Dy(III) systems. These models were based on the structures determined through X-ray experiments. The analysis was carried out using OpenMolcas and the SINGLE_ANISO programs,[62–66] replacing one of the Dy(III) ions with diamagnetic Y(III). Tables S3–S6† present the lowest Kramer's doublets (KDs) and the g factors of $\mathbf{1}^{(I=5/2)}$ and $\mathbf{2}^{(I=0)}$. The effective g_z tensors for $\mathbf{1}^{(I=5/2)}$ (Dy1), $\mathbf{1}^{(I=5/2)}$ (Dy2), $\mathbf{2}^{(I=0)}$ (Dy1) and $\mathbf{2}^{(I=0)}$ (Dy2) are 19.5920, 19.5186, 19.5772, 19.5362 respectively, which are closely approaching the Ising-limit value of 20, indicating a significant uniaxial anisotropy of each Dy(III) fragment. Tables S7–S10† show wave functions, characterized by a definite projection of the total moment $|m_J\rangle$ for the lowest two Kramer's doublets (KDs) of individual Dy(III) fragments in both complexes. The findings explicitly reveal the non-equivalent nature of the two individual Dy(III) sites within each complex. Furthermore, due to the non-equivalent nature of the Dy(III) ions, the easy axes are also not colinear, with an angle of ~30° between the anisotropy axes (green arrows in Fig. 1a). The ground KDs for the Dy(III) fragments are all predominantly composed of $m_J = \pm 15/2$, and their first excited states

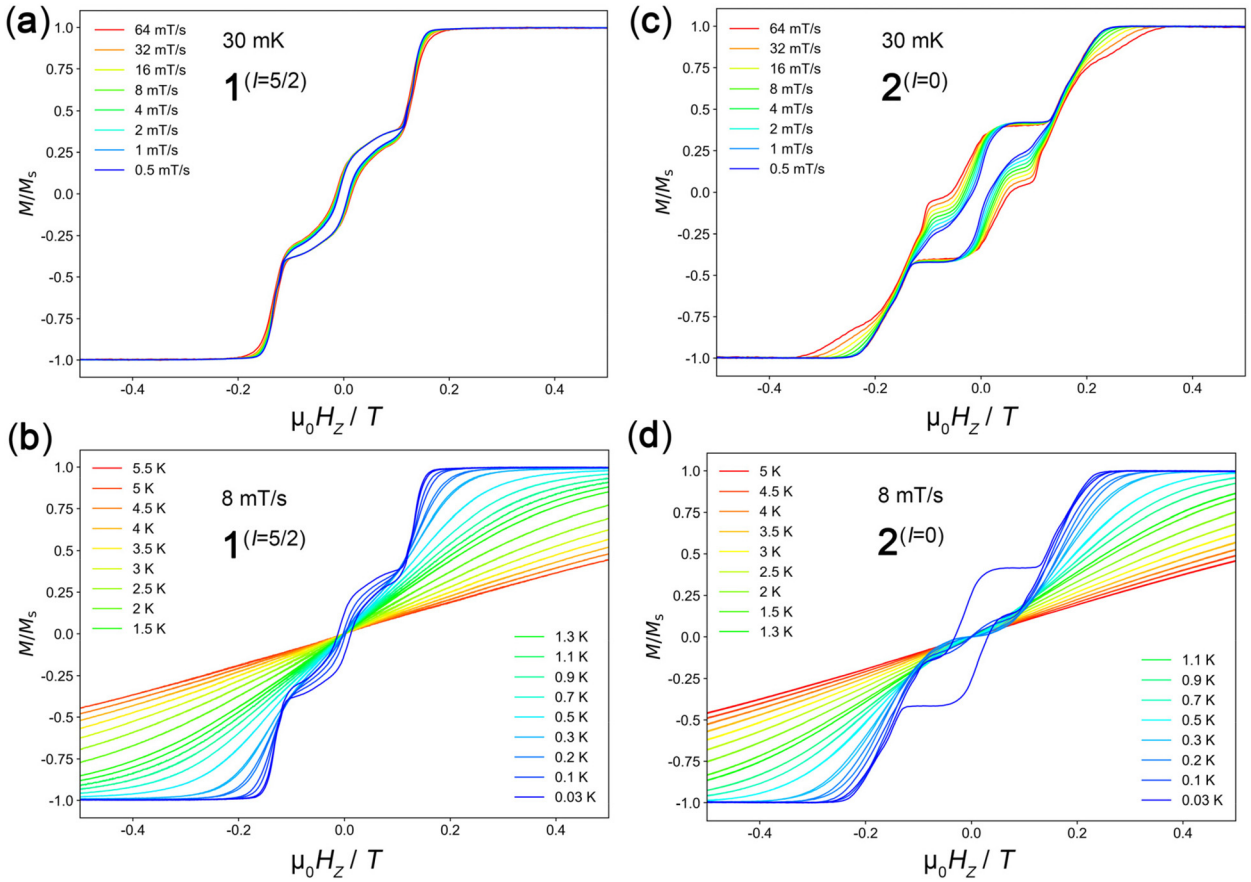

Fig. 4 Sweep-rate dependent μSQUID studies for (a) $\mathbf{1}^{(I=5/2)}$ and (c) $\mathbf{2}^{(I=0)}$ collected at 30 mK and temperature dependence of the μSQUID data for (b) $\mathbf{1}^{(I=5/2)}$ and (d) $\mathbf{2}^{(I=0)}$ collected at a sweep-rate of 8 mT s^{-1}.

are mostly composed of a mixture of several m_J states. The energy gaps between the ground and the first excited Kramer's doublet for each Dy(III) fragment are determined as follows: 91.7 K (64.2 cm^{-1}, Dy1) and 111.3 K (77.9 cm^{-1}, Dy2) in $\mathbf{1}^{(I=5/2)}$, 91.2 K (63.8 cm^{-1}, Dy1) and 121.7 K (85.2 cm^{-1}, Dy2) in $\mathbf{2}^{(I=0)}$. Notably, these gaps exceed the fitted barriers, suggesting the involvement of multiple relaxation processes in the relaxation.[67,68] The fitted $\tau^{-1}(T)$ corroborate the emergence of Orbach and Raman processes. Additionally, the transition magnetic moment matrix element for the ground state is comparable in both complexes, as depicted by the green line in Fig. S8,† while highlighting that the most viable relaxation pathway is through the first excited state.

The before-mentioned results showcase that for temperatures above 2 K, both relaxation mechanisms are not affected by the presence or absence of nuclear spins, while notable differences are visible at sub-Kelvin temperatures. The CASSCF obtained single-ion electronic characteristics show that relaxation is viable through the first excited state. However, although the magnetic anisotropy in Ln-SMMs complexes typically arises from individual Dy(III) ions, the slow relaxation dynamics of the complexes are notably impacted by interactions between Dy–Dy pairs, hence, the description of the relaxation must be that of dimeric species. To assess the interactions operating between the Dy(III) pairs, the $\chi_M T(T)$ and $M(H)$ were simultaneously fitted using the Lines model[69] as implemented in PHI.[70] The Lines model, employs an isotropic exchange between the spin component of the angular momenta of the Dy(III) ions ($S = 5/2$). A Hamiltonian of the following form was employed:

$$\mathcal{H}^i_{\mathrm{Dy}} = \mathcal{H}^i_{\mathrm{LF}} + g_J\mu_0\mu_{\mathrm{B}}(\hat{J}_{\mathrm{Dy}(1)} + \hat{J}_{\mathrm{Dy}(2)})\boldsymbol{H_z} + J^i_{\mathrm{Lines}}(\hat{S}_{\mathrm{Dy}(1)}\hat{S}_{\mathrm{Dy}(2)}) \quad (3)$$

where $\mathcal{H}^i_{\mathrm{LF}} = \sum_{k=2,4,6,-k\le q\le k} B^{\mathrm{q}}_{\mathrm{k}} O^{\mathrm{q}}_{\mathrm{k}}$ is the ligand field Hamiltonian expressed as Steven's operators ($O^{\mathrm{q}}_{\mathrm{k}}$), and $B^{\mathrm{q}}_{\mathrm{k}}$ are the ligand field parameters obtained from CASSCF. $\hat{J}_{\mathrm{Ln}}$, $\hat{S}_{\mathrm{Ln}}$ and g_J are the spin–orbit, spin-only state and Landé g-factor for Dy(III), respectively. The best simultaneous fits for $\mathbf{1}^{(I=5/2)}$ and $\mathbf{2}^{(I=0)}$ yields: J_{Lines} = +0.141(1) K (+0.098(1) cm^{-1}) for $\mathbf{1}^{(I=5/2)}$ and +0.178(1) K (+0.124(1) cm^{-1}) for $\mathbf{2}^{(I=0)}$. The Lines exchange fitted parameters can be projected onto the total spin of the Dy(III) ion, *i.e.*, ($J = 15/2$) leading to $J_{\mathrm{Lines}}(J = 15/2)$ = +16 mK (+0.01 cm^{-1}) for $\mathbf{1}^{(I=5/2)}$ and +20 mK (+0.014 cm^{-1}) for $\mathbf{2}^{(I=0)}$.

Furthermore, the μSQUID loops reveal the exchange field (H_{ex}), with $H_{\mathrm{ex}} = J_{\mathrm{total}} m_J / g_J \mu_\beta$, where $m_J = 15/2$, $g_J = 4/3$ and μ_β is the Bohr magneton, which allows the extraction of the exchange interaction by identifying the inflexion points in the hysteresis loops. The derivative of the temperature-dependent hysteresis loops (Fig. 5) shows a tunnelling event occurring at ±0.130 T in $\mathbf{2}^{(I=0)}$, whereas, for $\mathbf{1}^{(I=5/2)}$, tunnelling is spread out over a ±0.200 T range. The total (exchange + dipolar) coupling can be estimated by examining the tunnelling event that occurs at ±0.130 T in $\mathbf{2}^{(I=0)}$, resulting in J_{total} = +15.5 mK (+0.011 cm^{-1}). This value is very close to the strongest component of the dipolar matrix (*i.e.*, J^{dip}_{zz} = +14 mK (+0.01 cm^{-1})) for a ^{164}Dy···^{164}Dy distance of 4.064(3) Å (see ESI section 1.5†) and to the J_{Lines}, all projected onto a $J = 15/2$ state, hence the interaction in the isotopologues is mainly dipolar.

Based on the Lines model, it is readily visible that the SMM character in $\mathbf{1}^{(I=5/2)}$ and $\mathbf{2}^{(I=0)}$ arises from the thermal population of the first excited state lying at ∼2 K above the ground state. In this scenario, relaxation occurs between the first excited coupled states and the second coupled excited state (at ∼90 K) *via* the Orbach mechanism (Table S15†). Note that experimentally obtained barriers are smaller than the separation gap between these two states, hence, the Raman process and QTM play a role (see Fig. 3b and d). At temperatures above 2 K, the relaxation dynamic is dominated by the strong exchange interaction operating between the Dy(III) ions, which shifts to relatively high fields (±0.130 T) the commonly occurring [at zero field] QTM.

Nevertheless, at very low temperatures the situation is different, as evidenced by the μSQUID loops. Below 2 K, the thermally mediated mechanisms are less efficient, and QTM becomes predominant. By understanding the magnetic characteristics at lower energy levels for $\mathbf{1}^{(I=5/2)}$ and $\mathbf{2}^{(I=0)}$, one can elucidate the specific impact of the presence or absence of nuclear spins in both complexes. The large Hilbert space of the isotopologues here studied and the number of parameters involved, *e.g.*, Ligand Field Parameters, g-values, Euler angles, nuclear spins and exchange interaction, a $J = 15/2$ makes the rationalization of the sub-Kelvin temperature data computationally expensive. Hence, to bypass this problem, the spin effective formalism ($S_{\mathrm{eff}} = \frac{1}{2}$) is invoked, with pure axial g-tensors *i.e.*, $g_{xx} = g_{yy} = 0$; $g_{zz} = 20$ and the Euler angles for each Dy(III) ion obtained from the CASSCCF calculations. Nonetheless, $S_{\mathrm{eff}} = \frac{1}{2}$, at first order, mixed strongly by transverse fields, prompting huge tunnelling splitting not representative $m_J = \pm 15/2$ states, thus, we employ a fictitious $S = 3/2$ systems with an arbitrarily large Zero Field Splitting (D) parameter $D = -100$ cm^{-1}. The g-values were maintained isotropic ($g_{xx} = g_{yy} = g_{zz} = 20/3$) since the anisotropy is projected on the ZFS, while the anisotropy of the D term was rotated employing the Euler angles obtained from CASSCF.

To initiate our low-temperature analysis, we first concentrate on the magnetic properties of the nuclear spin-free $\mathbf{2}^{(I=0)}$ system, for simplicity. The CASSCF results indicate that the single ion magnetic properties of the isotopologues are dominated by the spin–orbit coupling and the interaction with the ligands, yielding a large separation between the ground $m_J = \pm 15/2$ and the first excited multiplet. This allows us to define the complex as two isolated Ising spins coupled through an effective interaction $J_{\mathrm{total}}(\hat{S}_1 \cdot \hat{S}_2)$, where J_{total} is an effective coupling and $\hat{S}_1 \cdot \hat{S}_2$, are effective spin for each Dy(III). Hence, in the presence of an external magnetic field applied along the easy axis, the Hamiltonian for $\mathbf{2}^{(I=0)}$ is defined as:

$$^{164}\mathcal{H} = g_{\mathrm{eff}}\mu_{\mathrm{B}}\mu_0 H_z \sum_i^2 \hat{S}_i + J_{\mathrm{total}}(\hat{S}_1 \cdot \hat{S}_2) + \sum_i^2 \hat{S}_i \cdot D_i \cdot \hat{S}_i \quad (4)$$

The first term in (4) is the Zeeman term, the second one being the exchange interaction and the last one being the zero-

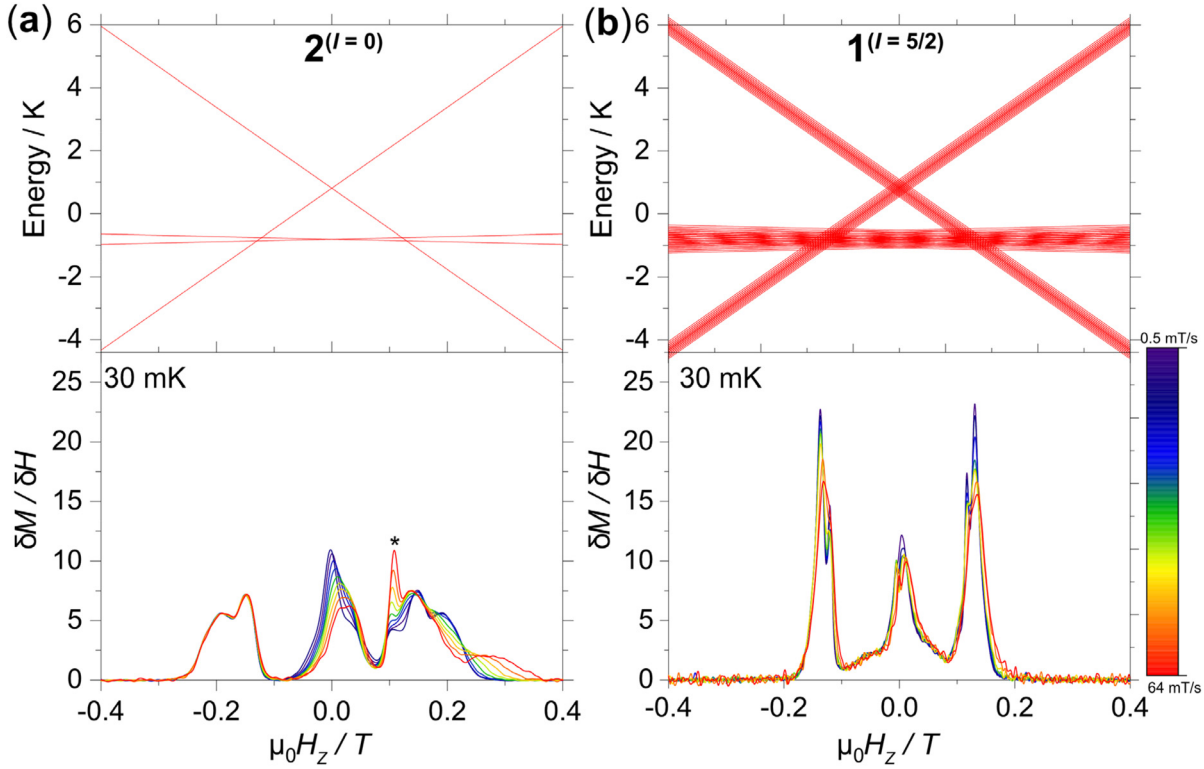

Fig. 5 Zeeman diagram obtained (top) and derivative of the temperature-dependent hysteresis loops from μSQUID studies (bottom) for (a) $\mathbf{2}^{(I=0)}$ and (b) $\mathbf{1}^{(I=5/2)}$.

field splitting. g_{eff} = 20/3 and J_{total} is the interaction between the ions (projected on a S = 3/2 basis). The non-colinear nature of the easy axes of the system is also taken into consideration by employing the Euler rotations [in Z–Y′–Z″ convention], as obtained from the CASSCF results (see ESI section 1.5†).

A crossing between the ground and the first excited state occurs at ±0.121 T when setting J_{total} = +15.5 mK (+0.011 cm^{-1}) as derived previously from the μSQUID exchange field. Refinement of the interaction to the crossing point at ±0.130 T yields J_{total} = 16.7 mK (+0.012 cm^{-1}). The difference between the J_{total} obtained from μSQUID studies and the values obtained by fitting the Zeeman diagram to the level crossing at ±0.130 T arise from the non-collinearity between the anisotropy axes of the Dy(III) ions.

Without an interaction operating between the Dy(III) ions, QTM would be active at zero field, as observed for most SMMs, with relaxation occurring also through the first excited state (*vide supra*). In contrast, the presence of an exchange interaction causes the zero-field crossing to shift towards larger fields (Fig. 5a). Furthermore, the interaction decreases the tunnelling transition probability within the ground doublet and the first excited coupled state since it would involve a double spin–flip process. Hence, for a field sweep from −0.5 T to +0.5 T the following processes occur: (i) at $\mu_0 H_z$ = −0.5 T (with the field chosen along the easy axis of the Dy(III) ions) the sample is polarized and all the spins are in the ground state |−15/2, −15/2⟩; (ii) as the magnetic field is swept from negative to the positive field, the molecules remain in the ground state until the external field compensates for the bias field and the spins make a transition from the ferromagnetic to the antiferromagnetic order by QTM. Notice that |±15/2, ∓15/2⟩ state is split in two due to the non-colinear arrangement of the easy axes, hence the crossings occur at $\mu_0 H_r \sim -0.110$ T and −0.130 T; (iii) the next crossing occurs at zero-field, where some of the spins that remain pinned to the ferromagnetic excited state can tunnel *via* the antiferromagnetic excited state |±15/2, ∓15/2⟩; and (iv) the last transition happens at $\mu_0 H_r \sim +0.120$ T where the molecules relax non-adiabatically from the state |±15/2, ∓15/2⟩ to |+15/2, +15/2⟩. As observed, in the case of $\mathbf{2}^{(I=0)}$, QTM occurs at the three intersections between the ground singlet and the excited doublet (∼±0.130 T), with the strongest transition occurring at the zero-field crossing.

Additionally, it must be noted that the $M(H)$ curves (at 30 mK) for $\mathbf{2}^{(I=0)}$ (Fig. 4c) exhibit thermal relaxation in addition to QTM, observed as a slow change in magnetization, clearly visible at faster sweep rates. In fact, in this case, thermal relaxation and QTM compete at such temperatures dramatically. While ramping the field from negative saturation towards positive saturation, a large population remains in the ferromagnetic state |−15/2, −15/2⟩ due to a small QTM gap at the crossings with |±15/2, ∓15/2⟩ at −0.120 T (see Fig. 5a). For faster sweep rates, a large fraction of this population remains pinned to |−15/2, −15/2⟩ even after crossing zero field, due to

a small QTM gap between states $|-15/2, -15/2\rangle$ and $|+15/2, +15/2\rangle$. Next, due to the direct relaxation events following the QTM event between states $|\pm15/2, \mp15/2\rangle$ and $|+15/2, +15/2\rangle$ around +0.110 T (possibly increasing the spin temperature), the thermal relaxation for the leftover population from the state $|-15/2, -15/2\rangle$ is triggered causing an avalanche of relaxation eventually to $|+15/2, +15/2\rangle$. This results in a large derivative for fast sweep rates at +0.110 T (see star in Fig. 5a). For slow sweep rates, this specific peak is smaller since most of the population could tunnel from $|-15/2, -15/2\rangle$ to $|+15/2, +15/2\rangle$ at zero field. Hence, the change in magnetization at +0.110 T is mainly due to QTM between states $|\pm15/2, \mp15/2\rangle$ to $|+15/2, +15/2\rangle$ and not enhanced by an avalanche of relaxation from the state $|-15/2, -15/2\rangle$. Eventually, a pure thermal relaxation event between states $|\pm15/2, \mp15/2\rangle$ to $|+15/2, +15/2\rangle$ is observed, which shifts towards higher fields for slower sweep rates, as evidenced by the last peak near positive saturation in Fig. 5a moving towards +0.3 T for slower sweep rates.[60]

In contrast, the $M(H)$ curve (at 30 mK) for $\mathbf{1}^{(I=5/2)}$ in Fig. 4a exhibits fast transitions at the crossing fields, as the curves at different sweep rates fall on top of each other indicating QTM-dominated transitions. The different relaxation behavior between Fig. 4a and c is attributed to the presence of nuclear spin in the latter and is discussed next. The four previously discussed processes [(i) to (iv)] also occur in $\mathbf{1}^{(I=5/2)}$. Contrary, however, $\mathbf{1}^{(I=5/2)}$ bears a nuclear spin capable of inducing hyperfine-QTM. The presence of a nuclear spin in $\mathbf{1}^{(I=5/2)}$ changes the form of the Hamiltonian, which now incorporates the hyperfine (A_{hyp}) and quadrupolar (P_{quad}) interactions as follows:

$$^{163}\mathcal{H} = {}^{164}\mathcal{H} + \sum_{i=1}^{2} A_{\mathrm{hyp}} \boldsymbol{I}^i \cdot \boldsymbol{\sigma}_i + P_{\mathrm{quad}} I_z^i I_z^i \qquad (5)$$

The Zeeman diagram for $\mathbf{1}^{(I=5/2)}$, as shown in Fig. 5b, was obtained by fixing J_{total} as for $\mathbf{2}^{(I=0)}$, while the hyperfine and quadrupolar interactions were fixed to A_{hyp} = 107.1 mK (0.074 cm^{-1}) [projected from an m_J = 15/2 to a S = 3/2 basis] and P_{quad} = 19.6 mK (0.014 cm^{-1}).

As depicted in Fig. 5b, in addition to the interaction between the Dy(III) centers, the Zeeman diagram shows $(2I + 1)^n$ hyperfine states with numerous crossings over a wider field range than for $\mathbf{2}^{(I=0)}$. Mainly at the crossings that conserve nuclear spin (*i.e.* $\Delta m_I = 0$), hyperfine-QTM is active, facilitating the relaxation of the system at a larger field span or causing the QTM occurrence to shift from ±0.130 T to various field values. This is evidenced in the much stronger *hf*-QTM shown at the ±0.130 T crossing compared to the crossing at zero field. Another effect that can enhance QTM further in such systems is the non-axial arrangement of the quadrupole tensor. For simplicity, the quadrupole interaction axis is assumed to be aligned with the ligand field axis and the interaction is uniaxial. However, generally, this axis can be tilted from the ligand field easy-axis. Moreover, the quadrupole term can be expandable to axial and non-axial terms.[71] Together with the inter ionic couplings, the exact quadrupole terms introduce transverse interactions in the spin Hamiltonian, which can explain QTM gap openings at crossings between the hyperfine states without conserving nuclear spin, *i.e.* $\Delta m_I \neq 0$. This yields further positions in the field for QTM events.[71] In our system, due to the larger field range/a greater number of positions in which *hf*-QTM is active, the electronic spins can tunnel with higher probabilities. Hence, a smaller number of spins remain pinned to the ferromagnetic excited state, causing a smaller number of spins to tunnel at the zero-field crossing occurring in the ferromagnetic excited state (see smaller derivative at zero field in Fig. 5b).

Conclusions

Utilizing a 1,2,4,5-tetrazine-based ligand, we have successfully synthesized and characterized two isotopologues of dinuclear dysprosium complexes, featuring the $^{163/164}$Dy isotopes. Both complexes exhibit an antiferromagnetic interaction between the lanthanide ions. Computational methods, as well as AC and μSQUID data, provide validation for the observed experimental behavior. Our results evidenced that a suitable exchange interaction can render both isotopologues high-temperature (>2 K) magnetic characteristics alike, and solely by performing sub-Kelvin studies the differences due to nuclear spin can be unraveled. Due to the intra-molecular coupling and small QTM gaps between the states, the Dy dimer isotopologue without nuclear spin shows a dramatic competition between thermal and QTM pathways of relaxation at 30 mK temperature. On the other hand, enhanced QTM is evident for the isotopologue with nuclear spin, attributed to many QTM pathways available by the hyperfine and nuclear quadrupole interactions. This phenomenon, as also observed previously in other similar systems,[40] can be utilized to enforce a purely antiferromagnetic (for Ising dimers) and cyclic/toroidal (for Ising trimers) ground state at low temperature without the need to enhance interionic coupling. While the observed slow magnetic relaxation primarily stems from single-ion relaxation, the results indicate that the exchange coupling between the lanthanide ions influences the relaxation mechanism at different temperature ranges. Albeit the coupling between the lanthanide ions remains modest, investigating analogous dinuclear systems becomes crucial for understanding the effect and strength of the interaction into the relaxation characteristics of SMMs.

Data availability

The data supporting this article has been included as part of the ESI.†

All the magnetic data was processed employing Origin Pro 2023. The Debye analysis and relaxation fits were also performed using Origin Pro 2023, while the $\chi_{\mathrm{M}}T$ susceptibility data was fitted employing PHI (*J. Comput. Chem.*, 2013, **34**, 1164–1175).

The Zeeman diagrams of the angular dependence of the μSQUID studies were obtained using Easyspin implemented in MATLAB (*J. Magn. Reson.*, 2006, **178**(1), 42–55).

Full crystallographic details can be found in CIF format: in the Cambridge Crystallographic Data Centre database (CCDC 2337590 and 2337589).†

Conflicts of interest

The authors declare no competing financial interests.

Acknowledgements

We acknowledge the DFG-CCR 1573 "4f for future" (project B3) and the Karlsruhe Nano Micro Facility (KNMF, **https://www.kit.edu/knmf**) for the provision of access to instruments at their laboratories. T. T. R. acknowledges the China Scholarship Council (No. 201806650008). A. M. acknowledges the Alexander von Humboldt (AvH) Foundation for a postdoctoral fellowship, a Grant-in-Aid for the JSPS Research Fellowship program, and the financial support by JSPS KAKENHI Grant Numbers JP22KJ3097 and JP23K13723. W. W. thanks the German Research Foundation (DFG) concerning the Gottfried Wilhelm Leibniz-Award, ZVN-2020_WE 4458-5. E. M.-P. thanks the Alexander von Humboldt fellowship for experienced researchers for support.

References

1 M. N. Leuenberger and D. Loss, *Nature*, 2001, **410**(6830), 789–793.
2 D. Aravena and E. Ruiz, *Dalton Trans.*, 2020, **49**, 9916–9928.
3 A. Gaita-Ariño, F. Luis, S. Hill and E. Coronado, *Nat. Chem.*, 2019, **11**, 301–309.
4 M. Atzori and R. Sessoli, *J. Am. Chem. Soc.*, 2019, **141**, 11339–11352.
5 G. Gabarro-Riera, G. Aromi and E. C. Sanudo, *Coord. Chem. Rev.*, 2023, **475**, 214858.
6 F. Paschke, T. Birk, V. Enenkel, F. Liu, V. Romankov, J. Dreiser, A. A. Popov and M. Fonin, *Adv. Mater.*, 2021, **33**, e2102844.
7 F. Paschke, T. Birk, V. Enenkel, F. Liu, V. Romankov, J. Dreiser, A. A. Popov and M. Fonin, *Adv. Mater.*, 2021, **33**, 2102844.
8 W. J. Xu, Q. C. Luo, Z. H. Li, Y. Q. Zhai and Y. Z. Zheng, *Adv. Sci.*, 2024, **11**, e2308548.
9 L. E. Darago, M. D. Boshart, B. D. Nguyen, E. Perlt, J. W. Ziller, W. W. Lukens, F. Furche, W. J. Evans and J. R. Long, *J. Am. Chem. Soc.*, 2021, **143**, 8465–8475.
10 D. A. Galico, E. M. Rodrigues, I. Halimi, J. Toivola, H. Zhao, J. Xu, J. O. Moilanen, X. Liu, E. Hemmer and M. Murugesu, *Nat. Commun.*, 2024, **15**, 3498.
11 D. Reta, J. G. Kragskow and N. F. Chilton, *J. Am. Chem. Soc.*, 2021, **143**, 5943–5950.
12 A. H. Vincent, Y. L. Whyatt, N. F. Chilton and J. R. Long, *J. Am. Chem. Soc.*, 2023, **145**, 1572–1579.
13 S. Thiele, R. Vincent, M. Holzmann, S. Klyatskaya, M. Ruben, F. Balestro and W. Wernsdorfer, *Phys. Rev. Lett.*, 2013, **111**(3), 037203, DOI: **10.1103/PhysRevLett.111.037203**.
14 M. R. Wasielewski, M. D. Forbes, N. L. Frank, K. Kowalski, G. D. Scholes, J. Yuen-Zhou, M. A. Baldo, D. E. Freedman, R. H. Goldsmith and T. Goodson III, *Nat. Rev. Chem.*, 2020, **4**, 490–504.
15 S. Thiele, F. Balestro, R. Ballou, S. Klyatskaya, M. Ruben and W. Wernsdorfer, *Science*, 2014, **344**(6188), 1135–1138.
16 F. Luis, A. Repollés, M. J. Martínez-Pérez, D. Aguilà, O. Roubeau, D. Zueco, P. J. Alonso, M. Evangelisti, A. Camón and J. Sesé, *Phys. Rev. Lett.*, 2011, **107**(11), 117203.
17 M. Martínez-Pérez, S. Cardona-Serra, C. Schlegel, F. Moro, P. Alonso, H. Prima-García, J. Clemente-Juan, M. Evangelisti, A. Gaita-Ariño and J. Sesé, *Phys. Rev. Lett.*, 2012, **108**(24), 247213.
18 C. Godfrin, A. Ferhat, R. Ballou, S. Klyatskaya, M. Ruben, W. Wernsdorfer and F. Balestro, *Phys. Rev. Lett.*, 2017, **119**(18), 187702.
19 C. Godfrin, R. Ballou, E. Bonet, M. Ruben, S. Klyatskaya, W. Wernsdorfer and F. Balestro, *npj Quantum Inf.*, 2018, **4**(1), 53.
20 K. Pramanik, Y.-C. Sun, P. Brandão, N. C. Jana, X.-Y. Wang and A. Panja, *New J. Chem.*, 2022, **46**, 11722–11733.
21 Y.-Q. Zhou, W. Deng, S.-N. Du, Y.-C. Chen, Z.-Y. Ruan, S.-G. Wu, J.-L. Liu and M.-L. Tong, *Inorg. Chem. Front.*, 2024, **11**, 1061–1069.
22 A. Palii, B. Tsukerblat, S. Klokishner, K. R. Dunbar, J. M. Clemente-Juan and E. Coronado, *Chem. Soc. Rev.*, 2011, **40**(6), 3130–3156.
23 T.-T. Ruan, E. Moreno-Pineda, M. Schulze, S. r. Schlittenhardt, T. Brietzke, H.-J. r. Holdt, S. K. Kuppusamy, W. Wernsdorfer and M. Ruben, *Inorg. Chem.*, 2023, **62**(37), 15148–15156.
24 Y. N. Guo, G. F. Xu, W. Wernsdorfer, L. Ungur, Y. Guo, J. Tang, H. J. Zhang, L. F. Chibotaru and A. K. Powell, *J. Am. Chem. Soc.*, 2011, **133**, 11948–11951.
25 Z. Zhu and J. Tang, *Natl. Sci. Rev.*, 2022, **9**, nwac194.
26 Z. Zhu and J. Tang, *Chem. Soc. Rev.*, 2022, **51**, 9469.
27 K. Liu, X. Zhang, X. Meng, W. Shi, P. Cheng and A. K. Powell, *Chem. Soc. Rev.*, 2016, **45**(9), 2423–2439.
28 T. Okubo, K. Himoto, K. Tanishima, S. Fukuda, Y. Noda, M. Nakayama, K. Sugimoto, M. Maekawa and T. Kuroda-Sowa, *Inorg. Chem.*, 2018, **57**(5), 2373–2376.
29 P. Chábera, Y. Liu, O. Prakash, E. Thyrhaug, A. E. Nahhas, A. Honarfar, S. Essén, L. A. Fredin, T. C. Harlang and K. S. Kjær, *Nature*, 2017, **543**(7647), 695–699.
30 D. I. Alexandropoulos, K. R. Vignesh, T. C. Stamatatos and K. R. Dunbar, *Chem. Sci.*, 2019, **10**(6), 1626–1633.
31 S. Goswami, H. S. Jena and S. Konar, *Inorg. Chem.*, 2014, **53**(14), 7071–7073.
32 M. A. Lemes, H. N. Stein, B. Gabidullin, S. N. Steinmann and M. Murugesu, *ACS Omega*, 2018, **3**(8), 10273–10277.

33 S. Patra, T. A. Miller, B. Sarkar, M. Niemeyer, M. D. Ward and G. K. Lahiri, *Inorg. Chem.*, 2003, **42**(15), 4707–4713.
34 X.-H. Bu, H. Liu, M. Du, L. Zhang, Y.-M. Guo, M. Shionoya and J. Ribas, *Inorg. Chem.*, 2002, **41**(7), 1855–1861.
35 M. A. Lemes, H. N. Stein, B. Gabidullin, K. Robeyns, R. Clérac and M. Murugesu, *Chem. – Eur. J.*, 2018, **24**(17), 4259–4263.
36 B. Li, X.-N. Wang, A. Kirchon, J.-S. Qin, J.-D. Pang, G.-L. Zhuang and H.-C. Zhou, *J. Am. Chem. Soc.*, 2018, **140**(44), 14581–14585.
37 J. Wang, S. Zhou, C. Chen, L. Lu, B. Li, W. Hu, A. Kumar and M. Muddassir, *Dyes Pigm.*, 2021, **187**, 109068.
38 T. J. Woods, M. F. Ballesteros-Rivas, S. M. Ostrovsky, A. V. Palii, O. S. Reu, S. I. Klokishner and K. R. Dunbar, *Chem. – Eur. J.*, 2015, **21**(29), 10302–10305.
39 P. Richardson, R. Marin, Y. Zhang, B. Gabidullin, J. Ovens, J. O. Moilanen and M. Murugesu, *Chem. – Eur. J.*, 2021, **27**(7), 2361–2370.
40 S. G. Tolshchina, G. L. Rusinov and V. N. Charushin, *Chem. Heterocycl. Compd.*, 2013, **49**, 66–91.
41 D. Hunter and D. G. Neilson, *J. Chem. Soc., Perkin Trans. 1*, 1985, 1081–1086, DOI: **10.1039/P19850001081**.
42 P. Alemany, D. Casanova, S. Alvarez, C. Dryzun and D. Avnir, Continuous Symmetry Measures: A New Tool in Quantum Chemistry, *Rev. Comput. Chem.*, 2017, **30**, 289–352.
43 E. Moreno-Pineda, M. Damjanovic, O. Fuhr, W. Wernsdorfer and M. Ruben, *Angew. Chem., Int. Ed.*, 2017, **56**(33), 9915–9919.
44 E. Moreno-Pineda, G. Taran, W. Wernsdorfer and M. Ruben, *Chem. Sci.*, 2019, **10**(19), 5138–5145.
45 M. Briganti, F. Santanni, L. Tesi, F. Totti, R. Sessoli and A. Lunghi, *J. Am. Chem. Soc.*, 2021, **143**(34), 13633–13645.
46 K. N. Shrivastava, *Phys. Status Solidi B*, 1983, **117**(2), 437–458.
47 F. S. Santana, M. Perfetti, M. Briganti, F. Sacco, G. Poneti, E. Ravera, J. F. Soares and R. Sessoli, *Chem. Sci.*, 2022, **13**, 5860–5871.
48 J. Wang, J. J. Zakrzewski, M. Zychowicz, Y. Xin, H. Tokoro, S. Chorazy and S. i. Ohkoshi, *Angew. Chem., Int. Ed.*, 2023, **62**, e202306372.
49 J. Flores Gonzalez, F. Pointillart and O. Cador, *Inorg. Chem. Front.*, 2019, **6**(4), 1081–1086.
50 G. Huang, X. Yi, J. Jung, O. Guillou, O. Cador, F. Pointillart, B. Le Guennic and K. Bernot, *Eur. J. Inorg. Chem.*, 2018, **2018**(3–4), 326–332.
51 Y. Kishi, F. Pointillart, B. Lefeuvre, F. Riobe, B. Le Guennic, S. Golhen, O. Cador, O. Maury, H. Fujiwara and L. Ouahab, *Chem. Commun.*, 2017, **53**(25), 3575–3578.
52 F. Pointillart, K. Bernot, S. Golhen, B. Le Guennic, T. Guizouarn, L. Ouahab and O. Cador, *Angew. Chem.*, 2015, **127**(5), 1524–1527.
53 F. Ortu, D. Reta, Y. S. Ding, C. A. P. Goodwin, M. P. Gregson, E. J. L. McInnes, R. E. P. Winpenny, Y. Z. Zheng, S. T. Liddle, D. P. Mills and N. F. Chilton, *Dalton Trans.*, 2019, **48**, 8541–8545.
54 F. Luis, M. J. Martínez-Pérez, O. Montero, E. Coronado, S. Cardona-Serra, C. Martí-Gastaldo, J. M. Clemente-Juan, J. Sesé, D. Drung and T. Schurig, *Phys. Rev. B: Condens. Matter Mater. Phys.*, 2010, **82**, 060403.
55 J. Flores Gonzalez, H. Douib, B. Le Guennic, F. Pointillart and O. Cador, *Inorg. Chem.*, 2021, **60**, 540–544.
56 J. Flores Gonzalez, B. Lefeuvre, B. Degraeve, O. Cador and F. Pointillart, *Dalton Trans.*, 2021, **50**, 11466–11471.
57 W. Wernsdorfer, N. E. Chakov and G. Christou, *Phys. Rev. B: Condens. Matter Mater. Phys.*, 2004, **70**(13), 132413.
58 M. Dolai, E. Moreno-Pineda, W. Wernsdorfer, M. Ali and A. Ghosh, *J. Phys. Chem. A*, 2021, **125**(37), 8230–8237.
59 J. Long, F. Habib, P. H. Lin, I. Korobkov, G. Enright, L. Ungur, W. Wernsdorfer, L. F. Chibotaru and M. Murugesu, *J. Am. Chem. Soc.*, 2011, **133**(14), 5319–5328.
60 E. Moreno-Pineda, S. Klyatskaya, P. Du, M. Damjanovic, G. Taran, W. Wernsdorfer and M. Ruben, *Inorg. Chem.*, 2018, **57**(16), 9873–9879.
61 S. A. Sulway, R. A. Layfield, F. Tuna, W. Wernsdorfer and R. E. Winpenny, *Chem. Commun.*, 2012, **48**(10), 1508–1510.
62 F. Aquilante, J. Autschbach, R. K. Carlson, L. F. Chibotaru, M. G. Delcey, L. De Vico, I. Fdez Galvan, N. Ferre, L. M. Frutos, L. Gagliardi, M. Garavelli, A. Giussani, C. E. Hoyer, G. Li Manni, H. Lischka, D. Ma, P. A. Malmqvist, T. Muller, A. Nenov, M. Olivucci, T. B. Pedersen, D. Peng, F. Plasser, B. Pritchard, M. Reiher, I. Rivalta, I. Schapiro, J. Segarra-Marti, M. Stenrup, D. G. Truhlar, L. Ungur, A. Valentini, S. Vancoillie, V. Veryazov, V. P. Vysotskiy, O. Weingart, F. Zapata and R. Lindh, *J. Comput. Chem.*, 2016, **37**(5), 506–541.
63 D. Ma, G. Li Manni and L. Gagliardi, *J. Chem. Phys.*, 2011, **135**(4), 044128.
64 P. E. M. Siegbahn, J. Almlöf, A. Heiberg and B. O. Roos, *J. Chem. Phys.*, 1981, **74**(4), 2384–2396.
65 L. F. Chibotaru and L. Ungur, *J. Chem. Phys.*, 2012, **137**(6), 064112.
66 L. Ungur and L. F. Chibotaru, *Chem*, 2017, **23**(15), 3708–3718.
67 S. Mondal and A. Lunghi, *npj Comput. Mater.*, 2023, **9**(1), 120.
68 A. Lunghi and S. Sanvito, *Sci. Adv.*, 2019, **5**(9), eaax7163.
69 L. F. Chibotaru and L. Ungur, *J. Chem. Phys.*, 2012, **137**(6), 064112.
70 N. F. Chilton, R. P. Anderson, L. D. Turner, A. Soncini and K. S. Murray, *J. Comput. Chem.*, 2013, **34**(13), 1164–1175.
71 G. Taran, E. Bonet and W. Wernsdorfer, *J. Appl. Phys.*, 2019, **125**, 142903.

